International Journal of Rock Mechanics & Mining Sciences 93 (2017) 138–151

Contents lists available at ScienceDirect

International Journal of Rock Mechanics & Mining Sciences

journal homepage: www.elsevier.com/locate/ijrmms

Experimental evaluation of a distributed Brillouin sensing system for detection of relative movement of rock blocks in underground mining

Behrad Madjdabadi[a,*], Benoît Valley[b], Maurice B. Dusseault[c], Peter K. Kaiser[d]

[a] Department of Civil and Environmental Engineering, University of Waterloo, Waterloo, Ontario, Canada
[b] Centre for Hydrogeology and Geothermics, University of Neuchâtel, Neuchâtel, Switzerland
[c] Department of Earth & Environmental Sciences, University of Waterloo, Waterloo, Ontario, Canada
[d] Bharti School of Engineering, Laurentian University, Sudbury, Ontario, Canada

ARTICLE INFO

Keywords:
Brillouin frequency shift
SMARTprofile™
DiTeSt™
Spatial resolution
Displacement

1. Introduction to deformation monitoring premise

Underground mining in highly stressed, hard rock masses is commonly accompanied by seismic events that are located close to mining, near active stopes and other excavations, most frequently within one diameter of the excavation boundary. However, as the extraction ratio increases or mines progress to greater depths, remote events have been observed at large distances from active mining, where the direct mining related stress changes are negligible. Events in different mining blocks cannot be explained by models involving stress redistribution processes alone.

Some authors[1] suggest that remote seismicity occurs where geological features, especially faults, intersect a mining zone. In order to generate seismic events, such faults have to be close to the critical stress state for slip under the existing regional stress field, such that even small perturbations in the local stress field could cause slip and generation of seismic slip event. Although large seismic events have often been observed and attributed to slip on pre-existing geological faults, it is hypothesized here that shear bands can form and develop over time during a mine's life. In other words, rock bridges can gradually be weakened as mined areas expand, and a discontinuity plane gradually coalescences, offering more kinematic freedom as mining develops.[2–4]

Based on records of distant events (> 100 m) that occurred at the Creighton Mine in Sudbury, Ontario, Kaiser et al.[3] raised the possibility that the interdependence of widely-separated seismically active areas could be explained by gravity-assisted, deformation-controlled process in the rock mass. They used a "train analogue" to describe the sequential movement of rock blocks from close to the mined boundary to remote distances. As soon as the train locomotive starts to move, the first wagon begin to displace but the displacement wave gradually propagates from the nearest attached car to the last car at the end of the train but with some retardations.[5] The retardation in displacement and the transfer of forces depends on the geometry of the car assembly and the characteristics of the couplings. Applying this analogy to a rock mass, understanding when and how much each individual block displaces provides important information about the displacement transfer rates and rock mass deformation pattern evolution. As shown in Fig. 1, knowing the displacement field between two or more openings experiencing seismic activity (e.g., along profile AA') is thus central to an improved understanding of the time, location, magnitude and probability of remote seismic event evolution. The train analogy presented in[3] is similar to the slider block model proposed by Burridge and Knopoff [6] to explain the temporal and spatial interrelationship between sequential earthquakes, showing how cumulative small events may eventually trigger larger events. The remote seismic events can either happen around large geological features such as fault if they are critically stressed (events around fault at Fig. 1) or they would be caused by the gravity driven deformation process of the rock mass moving toward mining stopes, as indicated by downward arrows in Fig. 1. Note that the microseismicity at A and A′ occurs because of significant stress change.

Conventionally, strain measurements in underground mining involve point sensors and displacement measurements are conducted

* Corresponding author.
E-mail address: bmollaha@uwaterloo.ca (B. Madjdabadi).

http://dx.doi.org/10.1016/j.ijrmms.2016.11.008
Received 23 November 2015; Received in revised form 17 June 2016; Accepted 13 November 2016
Available online 02 February 2017
1365-1609/

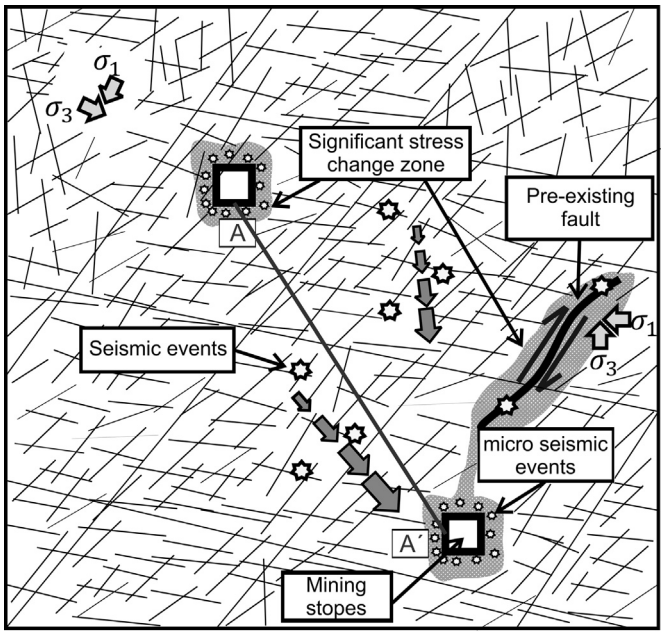

Fig. 1. Seismic events located remote from active mining areas might be associated with the rock mass movement toward openings over time with increases in extraction ratio (shaded areas highlight where the direct excavation-induced stress change might be significant). Continuous rock blocks displacement measurements between A and A′ could help understanding deformation-induced, remote seismicity.

with multipoint sensors such as extensometers allowing displacement monitoring between a limited number of anchors. These techniques are typically restricted to the near-field of excavations because of drilling and instrumentation limitations. Therefore, to study whether correlations exist between rock mass displacements and remote seismic events, would require new, far-field monitoring capability that could provide a comprehensive insight into the displacement field between openings and mining blocks (i.e., at the 10's to 100's of meters scale).

Recently developed distributed Brillouin sensing (DBS) systems are strain monitoring devices that, in conjunction with purpose-built fiber optic sensors, can provide a continuous strain field over large distances. They have been successfully applied in many engineering fields, e.g., for monitoring electrical power lines,[7] oil and gas pipelines,[8] coiled tubing,[9] concrete and steel bridges,[10–12] composite structures,[13] embankments and dams,[14,15] landslide activity and slope stability assessment.[16] They have also been used to monitor underground excavations including shallow tunnels [17] and underground mines[18–20] but not for the purpose described above.

In the present study, a DBS has been adopted for laboratory-scale testing to evaluate its capability and limitations for monitoring deformation patterns in long boreholes for mining application. The main objectives of this research include the DBS response to various deformation sequences and spatial configuration, the ability to detect joint opening with the sensing cable embedded in the borehole filler, the optimum installation method, and the effect of mechanical properties of the filler on the strain transfer process from host rock to the monitoring cable.

2. Working principles of DBS

The light sent into an optical fiber is scattered in all directions, with maximum losses in the backward direction. There are three types of light scattering in an optical fiber: Rayleigh, Brillouin, and Raman scattering. Among these kinds of light scattering, Raman and Brillouin scattering have found applications in measurements of distributed sensors. The scattered Raman light has a frequency shift in the range of ± 10–13 THz with respect to the incident light, whereas this is in the range of 10–13 GHz for the Brillouin scattering. The intensity of the Raman scattering light shows high sensitivity to temperature change (ΔT), making it a reliable and widely used temperature sensing system.[21]

In Brillouin scattering, the scattered light reaches a peak over its spectrum at a frequency shifted from the pulsed light, known as the Brillouin frequency shift, ν_B:

$$\nu_B = 2nV_a/\lambda_o \quad (1)$$

where, n is the effective refractive index of the fiber, V_a is the acoustic wave velocity in the fiber core, and λ_o is the vacuum wavelength of the incident light. Acoustic wave velocity is dependent on changes in temperature and density due to strain along the sensing fiber, as is the Brillouin frequency shift, given by

$$\nu_B = \nu_{Bo} + C_\varepsilon \Delta\varepsilon + C_T \Delta T \quad (2)$$

where ν_{BO} is the Brillouin frequency at the initial reading at a given (T, ε) condition, and $\Delta\varepsilon$ and ΔT are the stain and temperature variation at subsequent measurements, respectively. Brillouin scattering sensing is best for strain measurements and in principle can provide a spatial resolution around 1 m in a 50 km long fiber.[9,22] The resolution of the measurement can reach 1 °C for ΔT and 2×10^{-5} for $\Delta\varepsilon$.

Among available Brillouin scattering sensing technologies, two types are most commonly applied. The first works based on spontaneous scattering called Brillouin Time Domain Reflectometry (BOTDR) with a need to access only one end of the sensing cable. The other is a stimulated scattering system, called Brillouin Time Domain Analysis (BOTDA), which requires access to both ends of the sensing fiber.[23]

In a stimulated scattering method, BOTDA, a weak continuous light source called the probe beam is back propagated into one end of the fiber while a high amplitude pumped pulse is simultaneously sent into the other end. The stimulation process, i.e. gain, becomes maximized when the frequency difference between these two beams is equal to the Brillouin frequency shift. The gain process is accomplished through monitoring of the power transfer ratio from pump to probe beams at certain light frequencies in a step-wise manner. Thus the Brillouin gain spectrum can be locally reconstructed and interpreted when the gain as a function of frequency at any individual sampling point along the fiber optic cable is analysed.

The DBS system used for the present study is a BOTDA commercially known as DiTeSt™, manufactured by Omnisens SA. Table 1 gives the DiTeSt™ configuration used for measurements in the study. Furthermore, a special fiber optic cable, called SMARTprofile™ made by Smartec, was used as the sensing cable. The SMARTprofile™ is composed of two separate strain-temperature sensor pairs, S1-T1 and S2-T2. The strain sensors are embedded in a polyethylene (PE) thermoplastic jacket such that any external force to the jacket fully transfers to the fiber optic sensors. Temperature sensors are placed in a tube before embedding in the PE jacket to provide a strain-free condition.

3. From field to laboratory

The motivation to initiate this laboratory program came from an initial field installation in 2011.[24] Five SMARTprofiles™ were installed across a 1000 m deep, 25 m high sill pillar. Boreholes breaking through the pillar allowed access from sides of the pillar. Only five stopes of the pillar, which was in early stages of extraction, were mined out during

Table 1
DiTeSt™ configuration used in the measurements.

Spatial resolution	Sampling interval	Distance resolution	Frequency resolution	Frequency swap range
0.5 m	0.1 m	0.1 m	1 MHz	10.2–11.1 GHz

the monitoring period. All cables were pre-tensioned with 2 kg dead weight prior to grouting to ensure they were installed relatively straight in their boreholes as well as allowing for capturing either extension or shortening.

The data acquisition frequency was set for every thirty minutes, the time that was needed for DBS to acquire high-resolution data. However, data collection was intermittent for most of the monitoring period because of the harsh environmental conditions (dust and temperature) where the readout unit was located. Environmental control measures were successfully implemented and continuous data were acquired for a limited time period.

The data collected from one of the sensors showed a high Brillouin frequency shift change at the 1.5 m point in the lower part of the borehole through the sill, near the edge of the sill. This abnormal frequency change was the result of a rock block detaching from the back of the bottom sill. This interpretation was confirmed with results from a close-by multipoint borehole extensometer installed parallel to the sensing cable in the sill pillar. Also, optical televiewer images showed that a pre-existing fracture could be detected at the depth of interest. Apart from this anomaly, the Brillouin frequencies along the length of all boreholes were within the noise limits.[25] This in-situ test was of an opportunistic nature (sudden availability of boreholes in a mine section that would experience significant deformation), but the installation procedure was not well controlled and the intermittent recording precluded a satisfactory interpretation of the collected data. These field experiments motivated the development of the laboratory testing program reported herein. We are currently seeking further opportunity for a field trial that will benefit from the findings of this laboratory study.

4. Testing program

The test setup used in this study consists of three moving plates, and one fixed plate. Moving plates are equipped with two ball bearings to travel smoothly on shafts in both forward and backward directions independent of other plates. The SMARTprofile™ can be clamped to the plates to create different testing configurations; e.g. clamping to all four plates providing three cable sections with 50 cm strained length (L_G), to three plates to give two cable sections of 50 and 100 cm long, or tightened to only two plates to have one single section of the sensing cable with 150 cm strained length. The cables between clamps were pre-tensioned to different levels (varying from unstrained to several hundred με).

There are four blocks at the front and back of the moving plates; each having a 10 cm long fully thread hexagonal bolt. These blocks are meant to either apply a driving force to the plates or to prevent them from further movement. The plate movements were measured by accurate digital and dial gages. The sensing cable is passing through the testing system and is clamped on plates at four locations. Three of the plates can independently move longitudinally in two directions while the fourth one is fixed. Independent measurements of the plate movements are obtained with micrometric dial gages. The driving/stopper blocks permit controlling the displacement of the plate using full-thread hexagonal bolt. The overall length of the testing system is 150 cm permitting to strain three independent sensing cable section of 50 cm.

There are a number of factors controlled during laboratory testing but not in the field. An important factor is that the actuation in the laboratory is deformation controlled, whereas in the field there is no way of knowing the deformation (joint opening or shear displacement). Joint opening, closing or shear displacement in the field must be deduced (calculated) from Brillouin frequency shift changes which directly depend on induced displacement over a strained interval. Also, another critical aspect is that the rock mass in the field is heterogeneous, which may generate strain responses that are hard to interpret, compared to the homogenous laboratory condition. Even the temperature in a field installation will vary far more than in a laboratory (in our case T≈22 ± 0.2), where it is possible to operate at a constant temperature and therefore not have to correct readings for temperature. For these reasons, calibration must be carried out in a laboratory setting.

50 cm long strained sections, l, i.e. the distance between two clamping point, were chosen as this is currently the minimum spatial resolution, L_{SR}, available in the DiTeSt™. Accordingly, all strain events with a length larger than L_{SR} should be registered with full accuracy by the DiTeSt™ (although our experiments [25] showed that strain can be measured accurately even for strained lengths between 0.5 and 1.0-times L_{SR}). The base noise level was characterized by ± 77 με; therefore, with 50 cm strained length, an elongation of at least 0.0385 mm was required to be detected univocally by the system.

5. DiTeSt™ evaluation under tension

In this section, the DiTeSt™ response is evaluated when the SMARTprofile™ (the sensing cable) was clamped to the plates under different configurations and displacement scenarios. This section explains how the measurement system (DiTeSt™ and sensing cable SMARTprofile™) responded to different patterns of deformation in space and for various sequences of deformation events. In these tests the cable was directly put under strain by clamping it to the test setup plates, schematically shown in Fig. 2. Such system behavior characteristics are required prior to evaluating the system response when the sensing cable is placed in situations more representative of field installations in a borehole, e.g. with embedment of the sensing cable in a mortar filling material.

5.1. Spatial distribution of strain events

The strain pattern in a rock mass is likely heterogeneous with strain localization on planes of weakness like rock joints. Depending on the rock joints spacing relative to the spatial resolution of sensing system (in our case L_{SR} =50 cm), various spatial pattern of deformation can be expected. If the joints are relatively widely spaced, the strain induced by each joint will generate a distinct response in the measurement record, while if the joint spacing gets relatively narrow compared to the system resolution, the strain induced by multiple joints will interact and will be blended in a combined response.

The results presented here then aim at investigating effects of spatial distribution of such strain events. For this purpose, the test setup of was used in the configurations presented in Fig. 2. Two main cases were considered: 1) an interacting case with strained sections directly adjacent to each other, and 2) a non-interacting case with strain free sections. In the first case with closely interacting deformations, a 170 cm length of cable was clamped at four locations (each clamp has a width of 5 cm), as shown in Fig. 2(a). For the second case with well separated, non-interacting deformations, strain free cable

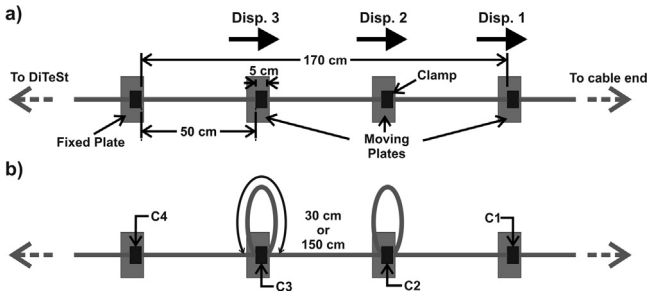

Fig. 2. Sensing cable configuration to study the response of the DiTeSt™ for different spatial distribution of strained events where they are located adjacent to each other (a) and when they are spaced at distances longer (or shorter) than the spatial resolution (b) of the system.

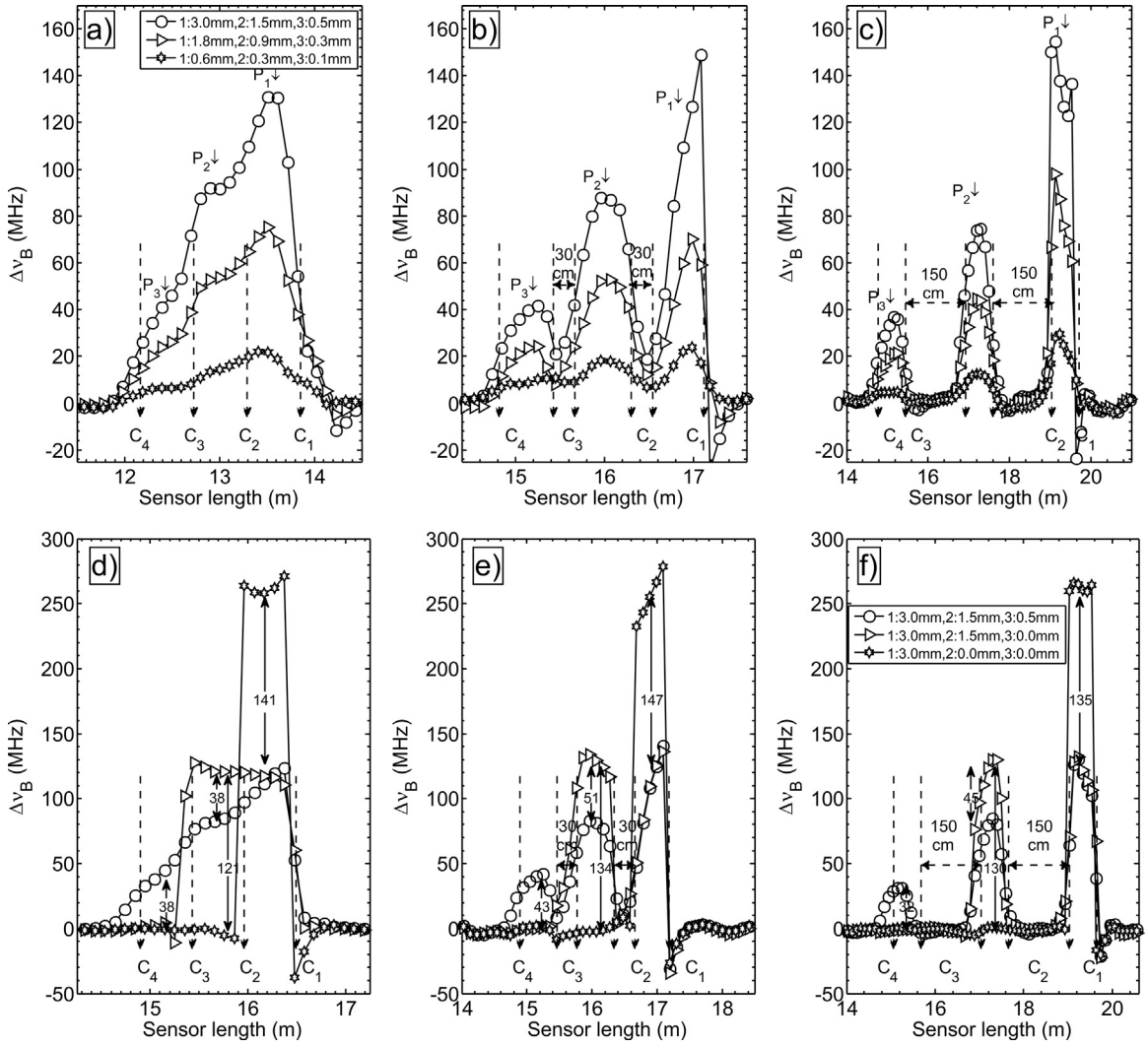

Fig. 3. Brillouin frequency shift change, $\Delta\nu_B$, for tests containing: a) zero, b) 30 cm, and c) 150 cm strain-free sections between the three successive strained intervals shown in Fig. 2. C_1–C_4 and P_1-P_3 represent the clamps location as shown in Fig. 1 and middle points along each strained interval. Sequential response of the DiTeSt™ for tests containing d) zero, e) 30 cm, and f) 150 cm strain-free sections.

loops were added between the strained sections (Fig. 2(b)). Strain-free loops of 150 cm (3 times the spatial resolution) were introduced to insure non-interactions. As an intermediate situation, a third case, was also considered with short strain-free loops of only 30 cm (less than the spatial resolution). In summary, the lengths of Fig. 2(a), 30 cm (intermediate case), and 150 cm (non-interacting case with two loops shown in Fig. 2(b)).

The displacement applied to each section was different from each other; the first, the second, and the third plates were displaced in five strain increments to a maximum of 3.0, 1.5 mm, and 0.5 mm, respectively (resulting in 1.5, 1.0, and 0.5 mm relative displacement). With a constant 50 cm strained length, this displacement scenario induced a strain level in the first section which was one and half times that of the second section and three times that of the third section, i.e. ε_1=1.5×ε_2=3×ε_3. This displacement sequence was chosen to induce three completely different strained intervals for better visual clarity in data presentation and calibration. These ratios were always kept constant at each steps.

Fig. 3 shows Brillouin frequency shift changes ($\Delta\nu_B$) relative to the unstrained state of the cable along the sensing cable for the three configurations. The location of clamps (C_1-C_4 in Fig. 2) is indicated as well as the strain-free sections. Fig. 3(a) shows the frequency (or strain) profile for a single continuous step-like strained section. Hence, the discrimination between three separate intervals is not be straightforward and depending on the applied displacement to each section. In other words, if equal displacement is applied to all three sections the final frequency profile is a continuous flat interval and it is difficult to discriminate between strained sections. In contrast, from Fig. 3(c) it can be seen that the strain profile identified three individually strained sections thanks to the separation by 150 cm long free-of-strain sections. Finally, Fig. 3(b) shows the intermediate situation with 30 cm long free-of-strain sections. Although there are clearly three strained sections, the free-of-strain section is not long enough to be uninfluenced by the straining. Therefore, with a 50 cm spatial resolution, a frequency change was detected over strain free lengths shorter than L_{SR}. In the latter two cases, the three individual strained intervals can be recognized even if the same strain is applied over each strained length.

Fig. 4 schematically illustrates what is actually happening in the case with 30 cm strain-free section. The Brillouin frequency shift change, $\Delta\nu_B$, at each sampling point, e.g. point p in Fig. 4(a) is computed over the spatial resolution, L_{SR}. Therefore, according to the set L_{SR}=50 cm and the 10 cm sampling interval for the DiTeSt™, five points including two points ahead and two points behind the point p contribute to the $\Delta\nu_B$ at this point. This is better understood when looking into the Brillouin gain spectra (BGS) at this point, Fig. 4(b). The frequency shift $\Delta\nu_B$ at each point is estimated as the peak gain function over a frequency range. At point p, the final registered gain is a

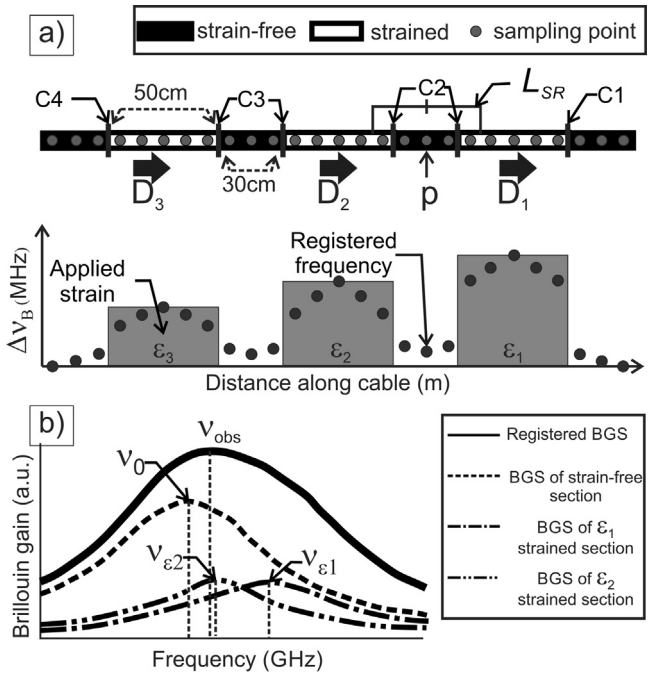

Fig. 4. a) A schematic presentation of $\Delta\nu_B$ at each sampling point along the cable for the test with 30 cm strain-free section; b) a typical registered Brillouin gain spectrum (BGS) at sampling point *P* located in the strain-free section. Final BGS at every sampling point like point *p* resulted from the contribution from all strained and unstrained sections. ν_O, $\nu_{\varepsilon 1}$, $\nu_{\varepsilon 2}$, and ν_{obs} represent frequency magnitudes at which unstrained, first and second strained section, and final BGS reached a peak over their corresponding spectra.

sum of three sub-gain functions associated with three different strained sections over the spatial resolution. The first gain spectrum peaked at ν_O corresponds to three points including point *p* located in the strain-free section, resulting in the largest sub-gain peak. Two other gain spectra peaked at $\nu_{\varepsilon 1}$ and $\nu_{\varepsilon 2}$ are recorded at far left and right points located in the first and second strained sections, respectively. These functions peak at the same gain amplitude but at different frequencies; a higher frequency corresponds to a higher strain. Finally, the resultant gain spectrum obtained from the summation of these gains peaked at a frequency (ν_{obs}) closer to the strain-free gain spectrum.

Fig. 5 presents graphs of $\Delta\nu_B$ against the applied strain for the middle point of each interval, indicated by P_1, P_2, and P_3 in Fig. 3 for the three configurations. The solid black line is the system manufacturer's correlation between Brillouin frequency shift change and applied strain, while the dashed line is the relationship based on tests performed by Madjdabadi et al. .[25] The error bars above and below each point in these figures represent the noise level of ± 3.8 MHz on $\Delta\nu_B$ typical for this system.[25] The measurements presented here are in agreement with the Brillouin frequency shift change to strain relation derived by Madjdabadi et al.[25] The proportion of the relative strain between each strained section, i.e. $\varepsilon_1=1.5\times\varepsilon_2=3\times\varepsilon_3$, were accurately captured by the system. These results confirm the validity of the linear correlation between the Brillouin frequency shift change and the independently applied strain regardless of the spatial pattern of deformation events.

5.2. Effect of deformation sequence

In the previous section, the spatial response of the system was evaluated whereby three individual adjacent sections were simultaneously strained. Another testing sequence was formulated to study the effect of strain sequence, loading path on the system response. In this case, every section was moved to its final displacement position before the next plate was moved. The first, second, and third plates were displaced to 3.0, 1.5, and 0.5 mm, respectively, similar to what was done in the spatial response tests. Such a deformation sequence was considered to study the DiTeSt™ behavior when rock blocks are sequentially open and close.

Fig. 3(d)–(f) shows the same three configurations as in the previous test, but as a result of the new straining sequence. These figure display the frequency profile at the final stage of each strained section; i.e. after moving the first plate to 3 mm, the second plate to 1.5 mm followed by displacing the third one to 0.5 mm. As expected, the frequency change response for the first (or the second) strained interval dropped almost as much as that of the second (or the third) strained interval increased.

Slight differences between frequency changes can be observed between loading steps (*L*) and unloading steps (*U*). They may be larger than the standard deviation of frequency change for repeated measurements of a constant strain over a strained length (error bars limits in Fig. 5). For example, in Fig. 3(f), straining the second section with a 1.5 mm displacement induced +130 MHz, while at the same time the first section was equally unstrained from 3 to 1.5 mm, but a larger

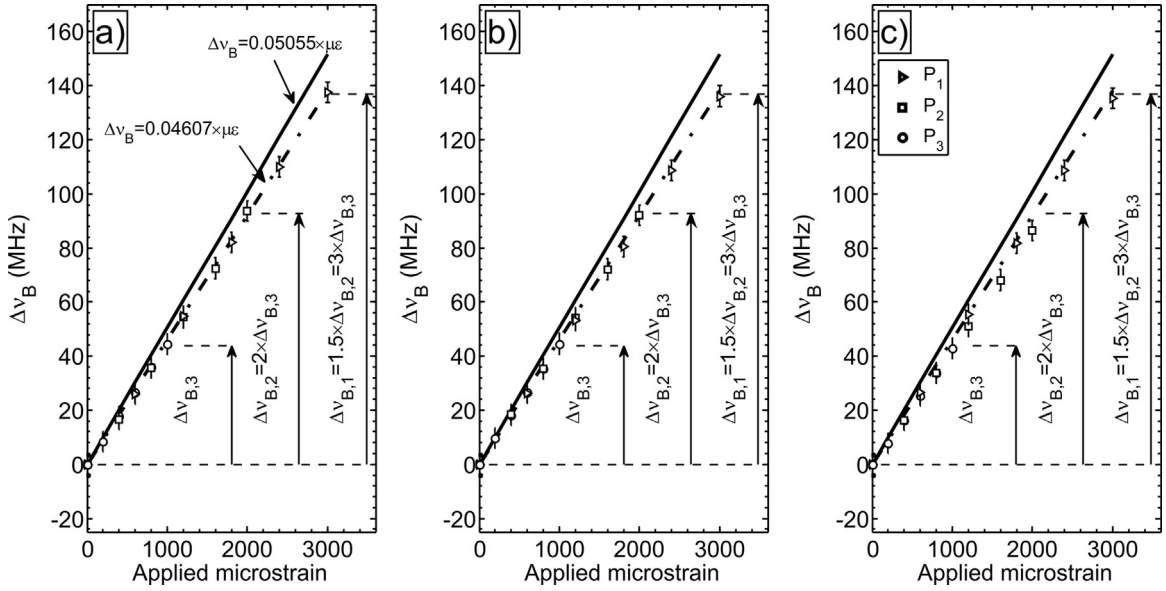

Fig. 5. $\Delta\nu_B$ against applied strain at three points indicated in Fig. 3(a–c) for tests containing a) zero, b) 30 cm, and c) 150 cm strain-free sections; showing good agreement with best-fit correlation determined by Madjdabadi et al.[25].

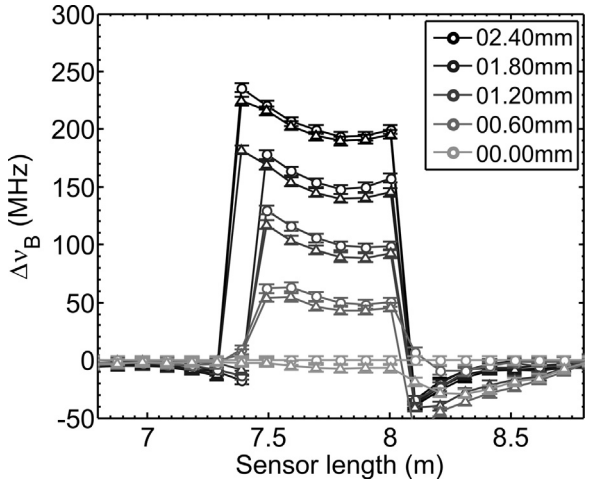

Fig. 6. The frequency difference over a 60 cm strained interval in loading (circles) and unloading (triangles) paths when the measurements were referenced to the first measurement.

reduction of 135 MHz was observed. Similarly, applying 32 MHz strain-equivalents (0.5 mm displacement) in the third section resulted in a relaxation of 46 MHz strain-equivalents in the second section.

The major contributor to this difference is thought to be associated with the systematic difference in the frequency response between loading and unloading of the cable. Three different lengths of the sensing cable (60, 80, and 100 cm) were subjected to 4000 με to better explore this system's behavior and the strain was then released in a step-wise manner. When all measurements were referenced with respect to the first zero reading, as shown in Fig. 6 for the 60 cm strained interval, the unloading associated graphs (triangles) showed less frequency shift compared with those from the loading path (circles). Even the final measurement, i.e. zero displacement in unloading path, registered a smaller frequency than first reading (frequency change for this final measurement was negative). Note that the frequency differences between straining and strain-relief paths are slightly larger than the base noise level (shown as error bars at each measurement point) of the system.

When plotting the frequency change at each point along the strained length for each test, it was noticed that all unloading associated frequencies, unrelated to location along the length, was slightly lower than those related to the loading path. The reason for this small difference remains unexplained. However, since it is a systematic rather than random factor and the difference was quite close to the base noise level, such a response did not affect the overall findings of the testing program.

6. Grouted sensor performance

As indicated in the introduction, for practial applications in long boreholes, it is important to understand the grout or Mortar-cable interaction. So far, the straining pattern and the effect of the straining sequence have been studied with direct extensional application of displacements to the sensing cable. However, for monitoring of the displacement field around underground mines, the cable must be placed in a borehole filled with a proper grout mixture.

In the following sections, the findings from experimentation with installation methods of the sensing cable are presented. The DiTeSt™ response was studied when the sensing cable was embedded in a mortar beam with the mix design given in Table 2. Tests included different embedment methods, the effect of joint spacing, and the effect of mortar thickness and strength on the strain transfer process. All tests were conducted on 2 m long mortar beams.

Table 2
Mix design for mortar beams including strong and weak mortars. The two mortar types were only different in the cement portion.

	Material	Cement	Lime	Sand	Water
Weight (kg)	Strong mortar	2.4	1.8	21.4	4.0–4.5
	Weak mortar	1.2	1.8	21.4	4.0

6.1. Embedment methods

Distributed optical fiber sensors have been installed in different ways in civil and geotechnical projects. They have been fully glued to steel girders,[12,26] placed within soil embankments[16] with the sensing cable attached to an inclinometer casing grouted into the soil [27] or attached by pins at a fixed spacing along a tunnel wall or concrete lining.[17,18]

The method by which the sensing cable is installed is very important in order to achieve a high performance monitoring response. In this study, the goal is to install the cable in a long borehole in a jointed rockmass, followed by grouting of the borehole. Two different installation approaches of the SMARTprofile™ sensing cable, motivated by the monitoring program objectives and DiTeSt™ limitations, were tested. In the first configuration, the bare cable was embedded in the filling material, i.e. the mortar beam, and its entire length was covered with grout. The second method included the anchoring of the cable at a specified spacing, the debonding of the cable section between each anchor pair using a debonding agent, and the grouting of the cable system (including anchors and debonded sections) into the mortar beams. Both these installation methods were studied to understand the optimum installation method for strain transfer in a mining situation.

6.2. Uncontrolled self-debonding for fully embedded case

A 38.1 mm×38.1 mm×2 m (width×height×length) beam was cast with the strong mortar mix design given in Table 2. The bare cable was entirely embedded inside the mortar to be in direct contact with the mortar, and pre-tensioned at each end with a 1 kg dead weight. After one week curing, the beam was placed on the moving table and clamped at three locations separated by 55 cm (Fig. 7) to simulate a rock joint opening process by inducing cracks into the mortar beam. In order to ensure that cracks would form at desired locations, a small notch at each crack location was created in the beam.

These three cracks were formed and opened based on a displacement sequence given in Table 3. The displacement scenario had one step for each moving plate. At each step, the plate of interest was moved to its final desired location (absolute displacements in Table 3). Then before the next plate was moved in the same manner, the first plate was fixed to the second plate in order to have a constant crack opening. The absolute displacement represents the amount of movement of each plate, whereas the relative displacement represents the corresponding crack opening for each plate. One measurement was

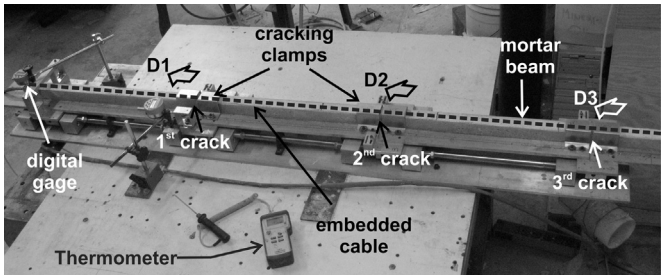

Fig. 7. Setup to test the deformation of the cable embedded in a mortar beam; cracks were induced at three 55 cm separated locations where the beam was clamped and different displacements (D_1–D_3) applied.

Table 3
Displacement sequence followed to induce three ongoing openinig cracks in the mortar beam.

Displacement step	1st plate displacement (mm)		2nd plate displacement (mm)		3rd plate displacement (mm)	
	Absolute	Relative	Absolute	Relative	Absolute	Relative
1	3.0	3.0	0	0	0	0
2	4.5	3.0	1.5	1.5	0	0
3	5.0	3.0	2.0	1.5	0.5	0.5

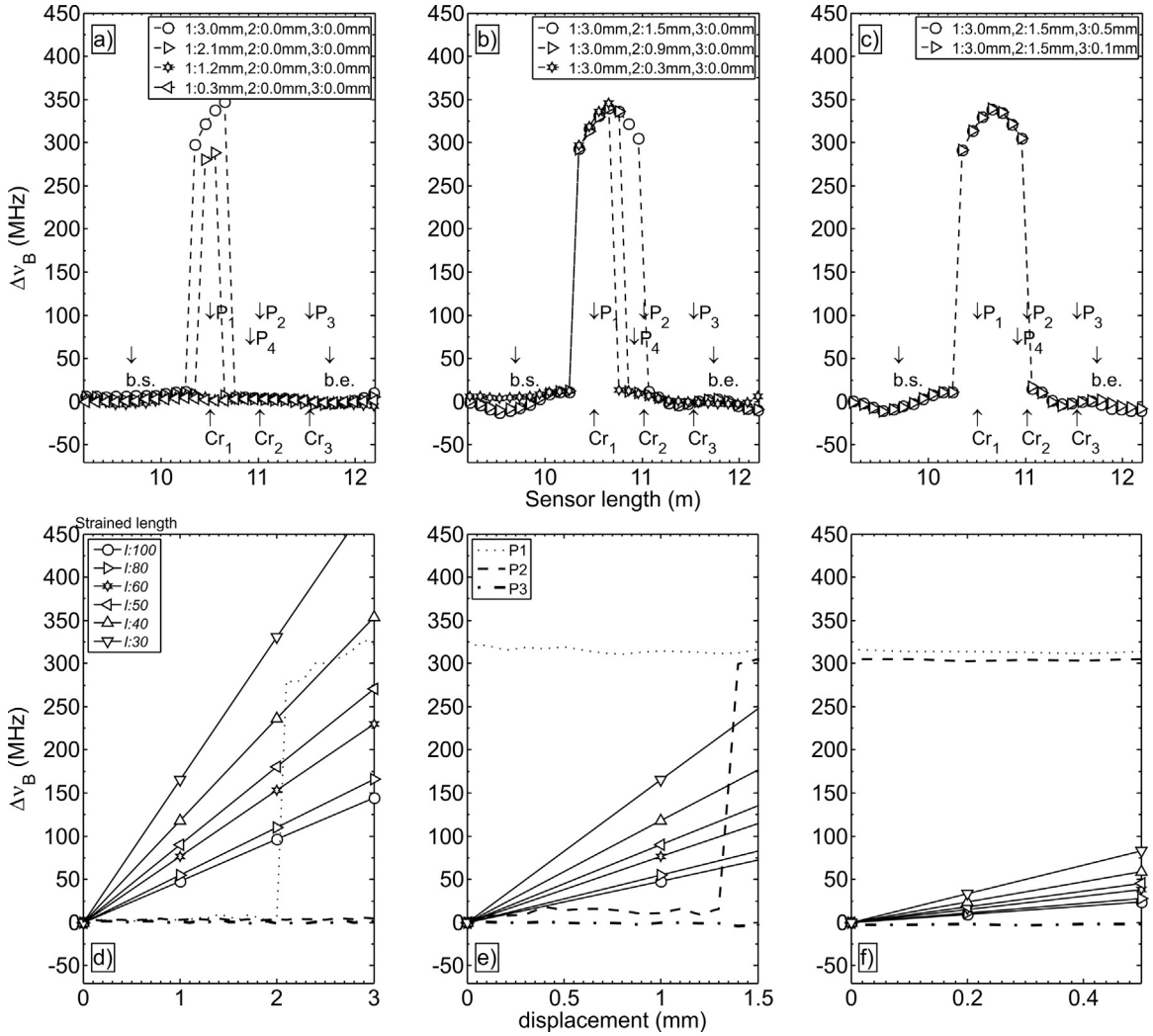

Fig. 8. Δv_B along the embedded cable in the mortar beam: after (a) the first, (b) the second, and (c) the third crack opened and was displaced. The most responsive step was when the first crack opened 2.0 mm, whereas the opening of the second crack only slightly affected the strained length of the cable. The frequency profile did not show any response upon opening of the third crack. P_1-P_3, Cr_1-Cr_3, *b.s.*, *b.e.*, and P_4 represents three points at the three cracks, beam start and end locations, as well as the point between Cr_1 and Cr_2 respectively. Δv_B against applied displacement for the three sampling points indicated in (a–c) at the first (d), second (e), and third (f) displacement steps. The cable debonding process could be followed at each displacement step. Lines with markers represent the best-fit lines between Δv_B and displacement for various assumed strained lengths.

recorded at every 0.1 mm displacement of each plate.

The main objective of this test was to understand the ability of the DiTeSt™ in crack detection in the mortar beam as well as registration of strain localizations due to crack opening at different locations along the beam with a fully bonded and embedded cable.

Fig. 8(a)–(c) shows the Δv_B relative to the initial state (i.e., with a pre-strained cable but an unstrained mortar beam) along the length of the sensing cable, where it enters and leaves the beam (indicated by *b.s.* and *b.e.* in Fig. 8(a)–(c)). At the first crack location, a visual inspection of the beam indicated that a crack was induced at displacements below 0.1 mm or so. However, the first detection of the crack opening at this location, point P_1 in Fig. 8(a), happened after 2.0 mm displacement. Before this movement had accumulated, no frequency response that could be attributed to strain localization was observed. At this displacement only 2 points, close to the first crack location, showed a clear frequency response. Increasing the crack opening from 2.0 mm to 3.0 mm caused a frequency profile response at two more points adjacent to the previous points.

After the first displacement step, the second plate was moved to 1.5 mm with a measurement every 0.1 mm. The second crack also formed at almost the same displacement as the first crack, but the frequency profile showed no change until 0.5 mm. From this displacement, the total number of points showing the frequency response increased gradually to seven as the relative opening of this crack

reached 1.5 mm. At step 3, although the crack was formed at a small displacement of 0.1 mm, the frequency profile did not change at all over 0.5 mm displacement of this plate.

The way DiTeSt™ responded to the applied displacement in this test was mainly controlled by the self-debonded length (the cable length that debonded from the mortar during displacement) of the sensing cable. Fig. 8(d)–(f) shows $\Delta\nu_B$ against the applied displacement corresponding to each individual crack at three different points located at the three crack locations, as indicated by P_1, P_2, and P_3 in Fig. 8(a)–(c) The six marked lines represent the best-fit linear correlation between $\Delta\nu_B$ and the applied displacement for six strained lengths obtained based on an extensional test on various lengths of SMARTprofile™.[25]

Since debonding occurs in an uncontrolled manner, the detailed interpretation of the measurements requires making assumptions about the debonded length at a given measurement time. Upon movement of the first plate at step 1 at the first crack location, the cable likely started to debond around the first crack. Since the system was not able to register any $\Delta\nu_B$ before the 2.0 mm crack opening, it follows that the self-debonded length was less than $L_{SR}/2$. However, as shown in Fig. 8(d), this length became sufficiently large (varying from 40 to 50 cm since $\Delta\nu_B$ followed the best-fit correlation lines associated with these strained lengths) for displacements above 2 mm such that $\Delta\nu_B$ was detected by DiTeSt™.

Similarly at step 2, the cable was likely self-debonding during all displacement stages, but the system at this crack location became responsive only at crack openings above 1.4 mm when the self-debonded section increased to more than 25 cm. Note that the $\Delta\nu_B$ at the location of the first crack, i.e. point P_1, remained constant during application of the displacement to the second crack, Fig. 8(e). This was expected from the displacement sequence given in Table 3, where the first crack opening was kept fixed during opening of the second crack. This also suggests that the two self-debonded lengths did not coalesce. For the third crack, in contrast to the other two cracks, no $\Delta\nu_B$ was detected by DiTeSt™ and we conclude that the self-debonded length never increased above $L_{SR}/2$ (Fig. 8(f)).

The strained length in this test was not fixed since the cable was detached from mortar in an uncontrolled self-debonding process. Although from Fig. 8(d–f) one can deduce the evolution of this length with applied displacement, the study of the Brillouin gain spectrum (BGS) at certain points along the sensing cable gives further insights in the behavior of DiTeSt™ specifically when some short strained lengths (here three self-debonded sections) are spaced with distances less than L_{SR}. Since the self-debonded length was shorter than L_{SR} during the initial opening phase of all cracks, the gain spectrum at points along this short length was different from a typical spectrum at points located along a strained length larger than L_{SR}. Where the spatial resolution covers points located in both strained and unstrained sections, two peaks would be registered in BGS at two different frequencies, one associated with the unstrained section and one related to the strained length. Actually, the final registered spectrum is a summation of the spectra of these two sections over the spatial resolution distance.

It has been noticed that the amplitude of BGS for both strained and unstrained sections for a strained length shorter than L_{SR} is dependent on the number of points within each section over spatial resolution interval. With a length ratio, r (varying from 0 to 1), defined as the self-debonded strained length, over the spatial resolution, two cases could happen. Where $r \leq 0.5$, i.e. the spatial resolution window included mostly the unstrained section, the BGS amplitude of this section was higher than that of the strained section. When the strain was below a certain limit, the BGS peak for the strained section occurred at frequencies quite close to that for the unstrained section. Since at this low strain level the self-debonded length was smaller than $L_{SR}/2$, the BGS peak for the strained section became hidden in the shoulder of that for the unstrained section (Fig. 9(b)). This resulted in a wider spectrum peaking at a frequency similar to that of the free-of-strain section, as shown in Fig. 9(a) for point P_1 located at the first crack for 0.2 mm displacement. At this displacement, the self-debonded length approximately covered only one sampling point, i.e. 10 cm, as sketched in Fig. 9(c).

At higher strain levels, the BGS for two unstrained and strained sections peaked at two different frequencies so that the final registered BGS showed two separate peaks, Fig. 9(d). Since the final BGS has a higher amplitude at the frequency of the unstrained section, the DiTeSt™ internal signal processing algorithm selected this frequency as the Brillouin frequency shift for this point at this displacement. According to the BGS for 1.5 mm opening of the first crack in Fig. 9(a), the self-debonded length of the cable was estimated to be 20–25 cm, as sketched in Fig. 9(e).

On the other hand, with $0.5 < r < 1$ at high displacements, more sampling points over the spatial resolution length fell within the strained section, so the BGS associated with the strained section showed a higher amplitude in comparison with that for the unstrained section, as shown in Fig. 9(f). Therefore, for all displacements above 2 mm, as shown in Fig. 9(a) for 3 mm opening of the first crack, DiTeSt™ detected a Brillouin frequency shift at the frequency of the strained section. In this case, the self-debonded length was found to have grown to 35–40 cm long, as sketched in Fig. 9(g).

The BGS for those points between the first and second crack location became even more complex when the second crack opened. This complexity was due to the short spacing (i.e. one spatial resolution length) between these events, i.e. cracks. For an example, for any point between the two cracks there are three different BGSs associated with each strained length over the spatial resolution, including an unstrained section and two self-debonded strained lengths at the first and second crack locations. The final registered BGS is a combination of all these three spectra.

Fig. 10(a) shows the BGS for a sampling point located between two cracks, as indicated with P_4 in Fig. 10(c). The registered BGS for this point already had two peaks even before starting the displacement of the second plate (circles in Fig. 10(a)). The higher peak belonged to the BGS for the unstrained section containing four sampling points, whereas the lower peak was due to one sampling point located in the self-debonded length of the first crack. During this test, the frequency at which BGS for the unstrained section and the first crack peaked remained constant during the formation of the second crack.

Upon the formation of the second crack, the self-debonded length at this crack was inferred to be about 10 cm, as shown in Fig. 10(c), where the third peak due to formation of the new crack was formed. However, at the early displacements with low strain levels the peak was hidden in the shoulder of the BGS for unstrained section, similar to the sketch shown in Fig. 9(b). At higher displacements above 0.4 cm, the amplitude of the observed BGS at frequencies about 10.66 GHZ increased, as shown in Fig. 10(a). This happened because at the current opening (i.e. 0.4 mm) the strain level was large enough so that the third peak moved away from that for the unstrained section, resulting in an almost flat spectrum between the peaks for unstrained section and first crack, as schematically shown in Fig. 10(b). Simultaneously, the peak amplitude for the unstrained section declined since one out of four points over the unstrained section was already strained due to the second crack. Nonetheless, since the BGS peak for unstrained section was still higher compared to the other two peaks, the Brillouin frequency shift was detected at a frequency close to this peak.

At the final displacement increment of the second crack, i.e. 1.5 mm, the observed BGS peaked at a frequency similar to the frequency of the BGS peak for the first crack, while the peak amplitude at frequency of the unstrained section decreased more (stars in Fig. 10(a)). The reason the final BGS peaked almost at the first crack frequency was twofold. First, applying more strain (in this case for displacements above 1 mm) moved the BGS peak associated with the second crack to the right at a frequency close to that of the first crack, as shown in Fig. 10(d). Also, this strain increased the self-debonded

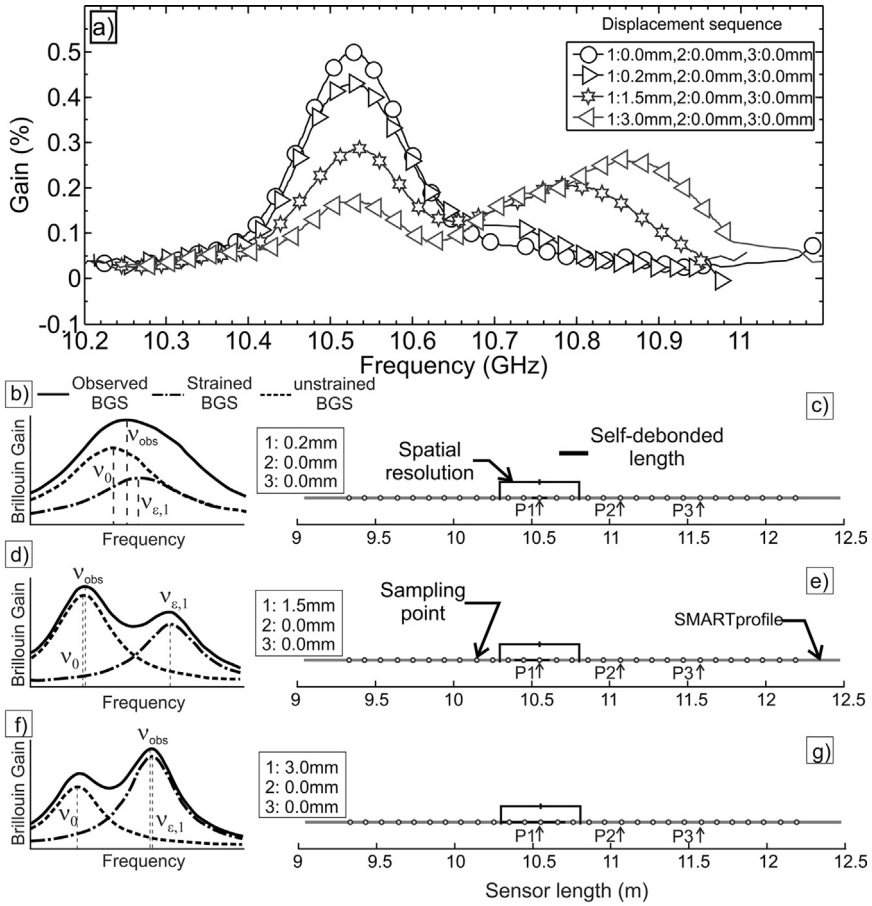

Fig. 9. a) Brillouin gain spectra of the point P_1 loacted at the first crack location for three different displacement steps. The registereded BGS at these displacement steps are schematically presented (b, d, f) where the contribution of various BGSs due to each strained section in the final BGS was noticed where the strained intervals had a spacing less than L_{SR}. Also, evolution of the self-debonded length during these displacement steps (c, e, g) were approximated using the BGS information. Curves in (a) has been smoothed using a moving average filter with a 5-point span for the sake of better presentation. ν_0, $\nu_{\varepsilon,1}$, and ν_{obs} represent the Brillouin frequency where the peak gain for unstrained, strained sections and observed measurement, respectively.

length around the second crack to less than 25 cm, covering two sampling points (Fig. 10(e)). Therefore the resultant BGS, as a summation of all BGSs, eventually peaked at a frequency close to those of both strained sections. It is interesting that although the second self-debonded length was less than $L_{SR}/2$ and from previous results no frequency response was expected, the presence of another strained section at a distance of $L_{SR}/2$ to the sampling point of interest, i.e. P_4, in the self-debonded length could increase the detectability of the system for the short length events.

With respect to the third crack, the applied displacement could finally induce a debonded length of around 10 cm covering only one sampling point. Such a small strained length was not able to create a high amplitude BGS so as to cause the registered BGS peaks at the frequency of the strained section.

It follows from this test that if the strained length is larger than L_{SR} and the sampling point is at least $0.5\times L_{SR}$ away from each end of the strained section, then one spectrum would be present in the observed BGS. As the strained length decreases to lengths below L_{SR} or the spacing of events of different strain levels is less than L_{SR}, then more than one spectrum become involved in the formation of the final registered BGS, which makes identifying an appropriate precise frequency more difficult. This is important with a full embedment installation of the sensing cable because not only the strained length (self-debonded length) varies with more crack opening, but also with presence of more cracks over the spatial resolution, short self-debonded sections are created close to each other.

Note that with the self-debonding cable installation method the DiTeSt™ can detect frequency changes due to crack opening as long as the self-debonded length increases to values above $L_{SR}/2$. Furthermore, there would not be a loss in strain transfer, therefore not only a qualitative but also a rough quantitative estimation of the joint movement could be established. However, non-constant strained lengths due to uncontrolled debonding and the presence of various events at close distances could affect the estimation of the real applied strain. Moreover, since the frequency change is linearly correlated with applied strain, in order to compute the crack opening the strained length should be fixed and known, thus with this installation method the relative block displacement assessment can include some uncertainties.

6.3. Controlled debonding with predefined debonded cable embedment lengths

6.3.1. Base case with three equal anchored lengths

From the primary evaluation of the DiTeSt™,[25] it was found that the minimum required strained length in order for the DiTeSt™ to be responsive was 30 cm, since the strained lengths below half the spatial resolution, i.e. $L_{SR}/2$=25 cm would not register any frequency change along the cable length. This was also confirmed in the test presented in Section 6.2. These results and the difficulty in interpreting the result from measurement where uncontrolled self-debonding occurs suggest that an alternate installation method with defined debonded lengths should be tested to controlled and always kept above $L_{SR}/2$.

The idea of this alternative installation method is to have anchoring

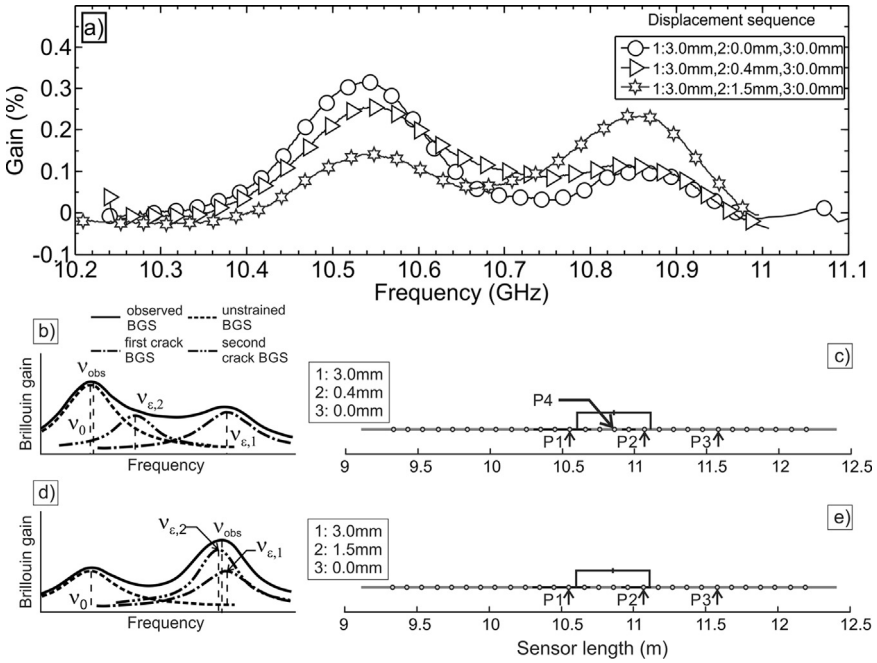

Fig. 10. a) BGS for the point P4 between the first and second crack locations for three displacement steps. The schematic reconstruction of the final BGS showed the contribution from three BGS's associated with two strained interval and one unstrained section at low (b) and high (d) strain levels during which the self-debonded length grew from 10 cm (c) to less than 25 cm (e), respectively. Curves in a has been smoothed using a moving average filter with a 5-point span for the sake of better presentation. ν_0, $\nu_{\varepsilon,1}$, $\nu_{\varepsilon,2}$, and ν_{obs} represent the Brillouin frequency where the peak gain for unstrained, first and second strained sections, and observed measurement, respectively.

points along the cables with pre-debonded cable in between. For this purpose, a 2 m length of the cable was first coated with petroleum jelly and wrapped with a plastic film to ensure that the length in between anchors are pre-debonded from the mortar. Then anchors were placed every 50 cm along the cable. Anchors are aluminum blocks with a narrow slot just under 4 mm width (i.e. less than the cable thickness) that can be easily mounted on the cable and tightened. In total, four aluminum anchor blocks were along the test length of the cable, which was then cast with the strong mortar (Table 2). In this test, only one joint was present in every anchored interval, therefore the effect of combined movement of multiple joints over one interval was not considered for the sake of simplicity and clarity.

The same displacement scenario was followed as given in Table 3. Fig. 11(a) shows the results of the tension test on this beam after inducing three cracks at a spacing of 55 cm. All cracks were formed at a displacement below 0.1 mm. It was found that the DiTeSt™ could register a frequency change just at the onset of crack development at displacements as low as 0.1 mm. Furthermore, the frequency profile clearly shows three individual strained sections according to the applied displacement sequence corresponding to each joint opening over each interval. This is important in that the frequency change could be related directly to the magnitude of joint opening or closure (this is the case because the strained length, i.e. pre-debonded anchored interval, is fixed, not only the induced strain in the cable. This was not possible with the previous method of installation.

Fig. 11(b) shows the BGS for a point located in the middle of the first interval, indicated as P_1 in Fig. 11(a). This figure includes three displacement states associated with the unstrained beam (circles), 0.1 mm crack opening (triangles), and maximum applied opening (stars). In contrast to what Fig. 9 showed for the self-debonding method, even at the minimum applied displacement of 0.1 mm, when the crack just formed, the final gain spectrum showed a clear single peak. Therefore where the pre-debonded length in this cable embedment method is equal or longer than L_{SR}, the gain function is constructed accurately.

Fig. 11(c)–(e) shows the $\Delta\nu_B$ with applied microstrain at three different points located in the middle of each interval, indicated as P_1, P_2, and P_3 in Fig. 11(a). These graphs are different from their corresponding ones for the test shown in the Section 6.2 with the self-debonding cable embedment method. For this figure, since the strained length was already known and constant, strain instead of displacement was considered against the frequency change. As shown in the figure, the frequency changes registered at all three points perfectly follow the linear best-fit from the beginning to the end of the applied strain.

6.3.2. *Influence of anchor/joint spacing*

In the test presented in Section 6.3.1 only one crack was induced per anchor length and opened according to a controlled displacement sequence. The $\Delta\nu_B$ profile and its linear correlation with strain was therefore purely influenced by this single crack. However, it is possible that there are several joints present within each interval, depending on either joint spacing or strained length (i.e. anchor spacing). For this reason, a beam with the high strength mortar mix was built and cured. The embedded sensing cable was anchored at two locations to ensure forming a strained length of 150 cm and it was coated with petroleum jelly before covering its entire length of the cable with a plastic heat shrink tube, similar to the debonding method used in Section 6.3.1.

Using the same setup, three cracks were induced within the beam every 55 cm over the pre-debonded anchored interval of 150 cm. For direct comparison, the same displacement sequence given in Table 3 for each moving plate was adopted. The main objective of this test was to understand how the DiTeSt™ would respond when strain localization occurred in terms of tensile cracking at several locations over a debonded length (anchored interval) that was larger than the joint spacing.

A hairline crack was formed at each crack location at displacements below 0.1 mm. Fig. 12(a) shows the $\Delta\nu_B$ relative to the initial unstrained beam along the length of the cable where it enters and leaves the beam. Solid horizontal lines show the expected frequency shift taking into account the actual applied strain based on a conversion factor of 0.4607 MHz/με and assuming the applied displacements are distributed over the entire debonded length. Upon movement of the first plate, even a 0.1 mm crack opening could be detected by the

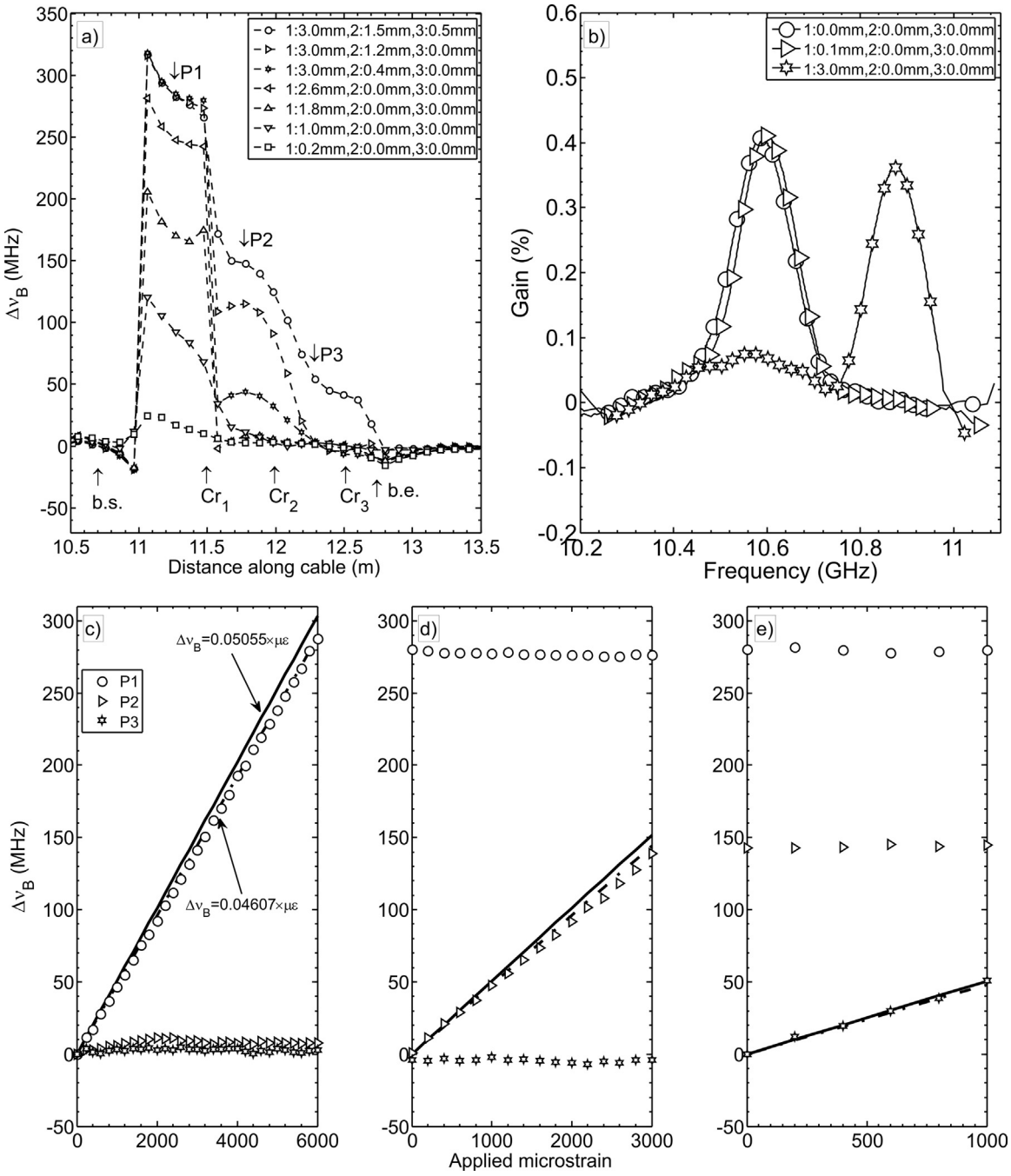

Fig. 11. a) $\Delta\nu_B$ for the debonded cable embedment method. The full gage length is mobilized at the early displacement stage. P_1-P_3, Cr_1-Cr_3, and *b.s.*, *b.e.* represent three points in the middle of each strained section, three cracks, beam start and end locations, respectively. B) BGS for point P_1 shown in (a) peaked at its maximum amplitude whether at low or large crack opening. Curves have been smoothed for the sake of better presentation. $\Delta\nu_B$ against applied strain for three points at the middle of each anchored interval at the first (c), second (d), and third (e) displacement steps showed good agreement with best-fit correlation lines.

DiTeSt™ uniformly over the length of the anchored length. The profile over the strained length was almost uniformly flat with no localized peak at the crack locations (Cr_1–Cr_3).

Furthermore, Fig. 12(b)–(d) give the variation of Brillouin frequency change with applied strain at the points indicated in Fig. 12(a), 50 cm separated from each other. The frequency variation at each of these three points followed quite closely the best-fit dashed line. It was noticed that where a perfect cable debonding from mortar occurs it would not matter how many joints exist over an anchored interval of the cable and in what order they open or close. The resulting profile would be an average of displacement at all joints over the strained length.

It is worth noting that the quality of the debonding was also an influential factor on the DiTeSt™ efficiency, particularly in a case similar to this test when more than one joint meet the anchored interval. If a low quality cable-mortar debonding exist, some strain localization would occur at crack locations resulting in a non-uniform frequency profile contrary to what is shown in Fig. 12(a).

6.3.3. *Influence of borehole diameter/filler thickness*

In the context of structural health monitoring, fiber optic sensors have been attached to the surface of the structure using a protective coating. However, it has been found that the mechanical characteristics of the protective bonding component influences the strain transfer

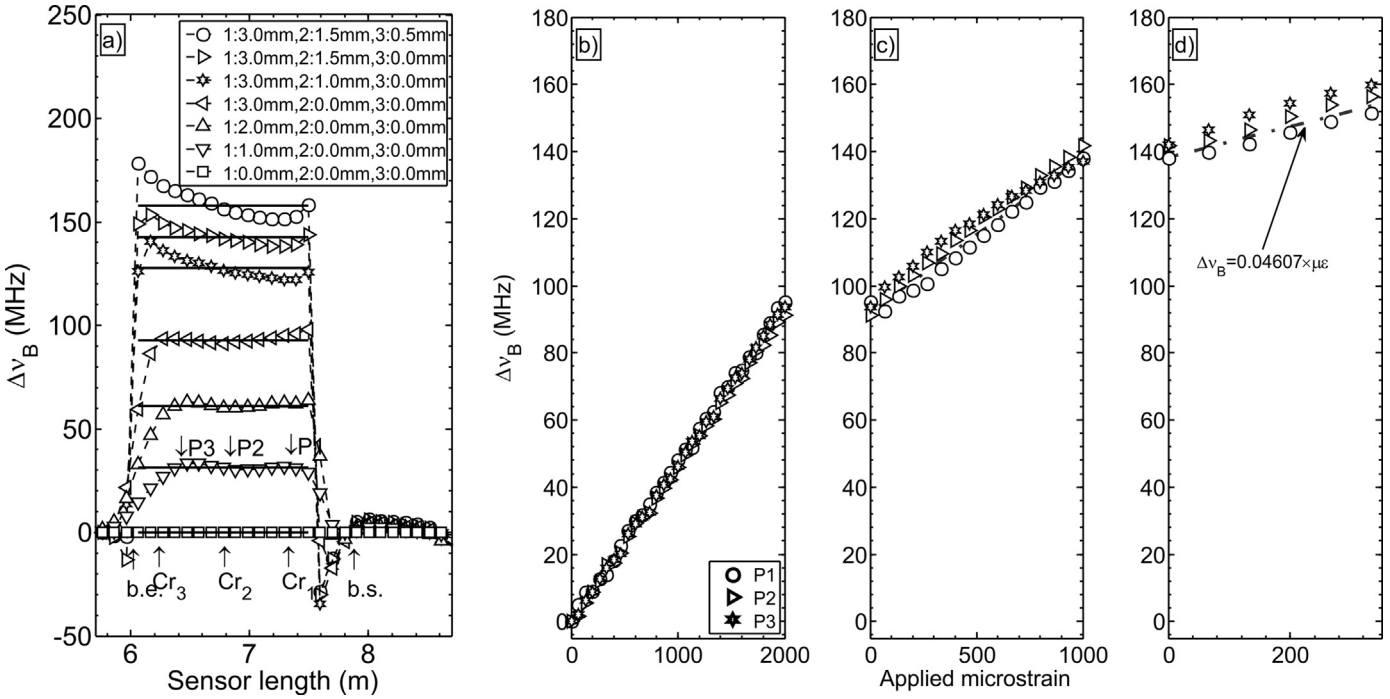

Fig. 12. $\Delta\nu_B$ along the cable (a), the evolution of $\Delta\nu_B$ over the course of the applied strain at three points (P_1–P_3) at the crack locations (Cr_1–Cr_3) at the first (b), second (c), and third (d) displacement steps for the 150 cm pre-debonded strained length of the cable. (b) to (d) shows that strain induced at each crack location has been uniformly distributed over the strained length because $\Delta\nu_B$ at these locations showed very good agreement with the best-fit correlation lines. The solid horizontal lines in (a) correspond to the theoretical applied strain over the anchored length.

process from the host material to the fiber optic, since a portion of the strain would be absorbed by the coating layer.[28] Furthermore, Wan et al.[29] showed that when a fiber optic sensor is bonded to the surface of a structure, the strain transfer process from the component of interest to the fiber optic sensor is influenced by additional factors such as bond length and thickness.

Distributed optical fiber sensors in an underground mine with our monitoring objective (far-field small strain measurements and joint dilation) would be installed in a borehole. The borehole diameter is mostly controlled by the underground equipment availability and capability. The thickness of the filling material would thus play a key factor in the transfer of the rock blocks movement and joint opening to the sensing cable and this is assessed next.

To explore this, a wider mortar beam of 50.8 mm square cross section was built with the strong mix design (Table 2) and cured for one week. The cable was coated with petroleum jelly and was anchored at four points along 2 m of the cable to create three 50 cm pre-debonded intervals. The testing procedure remained the same as before. The

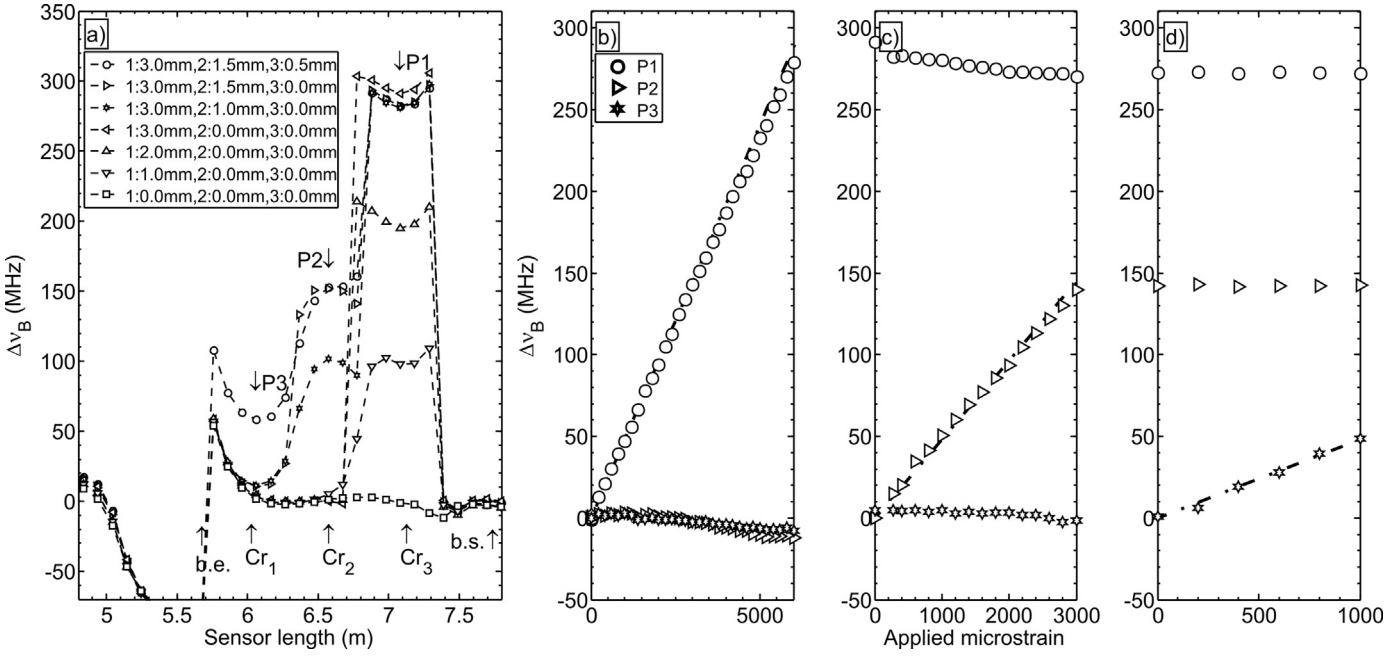

Fig. 13. $\Delta\nu_B$ along the cable (*a*), the evolution of $\Delta\nu_B$ over the course of the applied strain at three points (P_1–P_3) at the crack locations (Cr_1–Cr_3) at the first (b), second (c), and third (d) displacement steps for the thicker mortar beam did not show any difference with those with the smaller thickness beam.

displacement sequence given in Table 3 was followed and a tension crack was formed at each crack location at a displacement below 0.1 mm.

Fig. 13(a) shows the Brillouin frequency change, $\Delta\nu_B$, profile along the cable length (the cracks and beam end points have been indicated). Generally, the profile shapes are identical to those obtained with the smaller beam with a diameter or edge length of 38.1 mm. Further details could be noticed by plotting $\Delta\nu_B$ against the applied microstrain at each crack location at points P_1 to P_3, as shown in Fig. 13(b)–(d). It was found that the frequency change at these points at the middle of strained intervals perfectly followed the best-fit curve. The method used for cable embedment is certainly a key component in the cable response in this test, i.e. as long as the cable is debonded from the mortar, the thickness of the surrounding filler material in the borehole does not influence the sensing performance of the DiTeSt™.

6.3.4. Influence of filler material strength

In Section 6.3.3 it was explained that the mechanical characteristics of the bonding material could affect the strain transfer process. When backfilling the borehole with grout mix, its engineering properties should be accurately determined to confirm the conformance between the fiber and the surrounding rock.[30] The mixing procedure also affects the grout properties, and the ratio of water to cement is a key parameter for control of the grout strength.

It appears best to design a grout mixture for a borehole instrument to match its strength and deformation properties with the surrounding rock mass.[30,31] For an extensometer installation, it is better to use a grout type less stiff than the surrounding rockmass. This is so because if the stiffness of the grout is much larger than the rock, the deformation is mostly absorbed by the grout and less axial displacement would occur in the grout than the rock. For an inclinometer measurement, it is recommended to use a stiffer grout than the nearby rock to provide enough lateral confinement.[31]

The effect of the mortar strength on the measurement performance was studied here by reducing the strength by decreasing the cement portion from 2.4 to 1.2 kg (weak mortar mix in Table 3). One beam was cast with the cable anchored with 50 cm spacing and pre-debonded from mortar, and the same displacement steps for previous tests were adopted to induce three cracks over each anchored interval.

From Fig. 14(a), it was noticed that the frequency profile shape was identical to that in the test with stronger mortar beam. Furthermore, from Fig. 14(b)–(d), the Brillouin frequency shift change at three points in the middle of three anchored intervals closely followed the best-fit correlation. The results shown in this figure imply that with the adopted method of debonded cable embedment in the mortar, the mortar strength has no noticeable effect on the strain transfer process because the cable is fully debonded from the mortar along its length. With this installation method, the more important characteristics of the filling are the tensile strength as well as its placement performance in the borehole to fully cover the anchors.

7. Conclusions

Distributed Brillouin sensing systems (DBSs) have shown promising performance for continuous strain monitoring of large, complex, and dynamic structures such as bridges, dams, embankments, and tunnels. Another emerging field of application for such instruments could be in underground mining to establish the deformation patterns between excavations or mining blocks.

Since remote seismic events are often related active mining but cannot be explained by stress changes at far distances, a deformation controlled process of rock mass movement surrounding the mining zones might be useful to establish interactions between mining, induced deformations by gravity, and causal remote seismicity. Therefore, DBS instruments could potentially fill a gap in the understanding of the relationship between remote seismicity and far-field mine-wide displacement fields. To this end, an extensive experimental program was performed using a commercially available DBSs called DiTeSt™ in conjunctions with a sensing cable, SMARTprofile™, to study the spatiotemporal response of the monitoring system as well as the optimum borehole installation method and strain transfer process appropriate for monitoring relative rock block movement.

A sensing cable clamped at a certain length to moving and fixed plates of a test apparatus purposely built for these tests to create various strained section configurations to explore the spatial resolution of the system. The cable clamping configurations included three consecutive 50 cm sections with 0 cm, 30 cm, and 150 cm strain-free sections in between former sections. The applied displacement sequence chosen was applied through

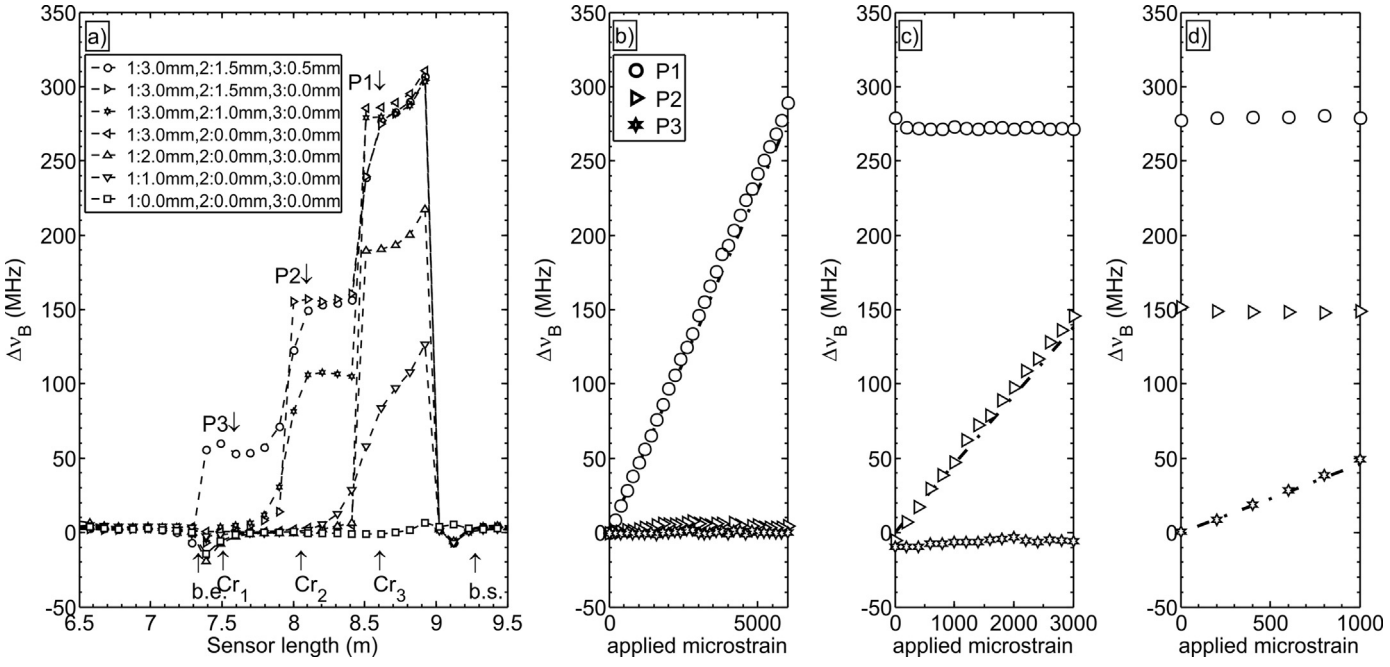

Fig. 14. $\Delta\nu_B$ along the cable (*a*), the evolution of $\Delta\nu_B$ over the course of the applied strain at three points (P_1–P_3) at the crack locations (Cr_1-Cr_3) at the first (*b*), second (*c*), and third (*d*) displacement steps for the weak mortar beam with the 50 cm spaced anchored cable showed the same performance as was noticed with the stronger mortar beam.

two different loading paths; in one experiment the displacements for each 50 cm section were simultaneously applied, whereas in the other scenario each section was strained when the previous one had already been strained to its maximum level. The DiTeSt™ could precisely show the spatial distribution of the strained sections. Furthermore, the frequency change response of the system was found to be independent of the loading path.

The installation method for the current objective of DiTeSt™ usage is borehole placement with grout filling. A major part of the experiments was to study the interaction between an embedded cable and the mortar beams (i.e. grout) and the effect of mortar properties on the strain transfer process.

When the cable was fully embedded in and bonded to the mortar beam, the DiTeSt™ response was different at each of three 55 cm spaced induced crack locations. This was found to be significantly influenced by the self-debonding length evolution with applied displacement. Apart from the positive point that the system could register frequency changes during cable debonding, the amount of crack opening could not be estimated with high accuracy since the strained length was not constant. The same test implemented with weaker mortar showed that the debonding process became more uncontrolled. Nevertheless, it was concluded that anchored and debonded cable sections could produce more meaningful results, i.e., results that can be interpreted without making many assumptions about strain transfer.

The cable was then anchored at 50 cm spacing and pre-debonded from the mortar between anchors. Inducing one crack over each anchored interval resulted in a totally different frequency compared to that in the fully bonded cable test. The frequency change registered over each interval was repeatable and consistent with the applied displacement since the strained length was constant.

The DiTeSt™ response was also evaluated with the presence of three cracks in the mortar beam over the strained length. With an imperfect debonded installation, one could actually approximate the number of the cracks in the interval and their opening sequence from the non-uniform frequency profiles, but this is not recommended because of other factors such as consistency in installation. On the other hand, a highly effective debonding method provides quite uniform profiles, but individual crack movements within an anchored interval could not be tracked.

Finally, the effect of filling thickness and strength on the strain measurement effectiveness were evaluated using a larger diameter beam and a beam formed with weaker strength mix, respectively. In both tests, DiTeSt™ showed exactly the same performance as with a smaller beam and stronger mortar. This is related directly to the cable embedment method in the mortar. Therefore, the most important characteristics of the filling material should be a low tensile strength so that it breaks at the joint locations as soon as they start moving.

The best method of installation based on the experimental studies on the sensing cable under pure tension should be the anchoring-debonding method with minimum 50 cm anchor spacing and a method to give high quality and complete debonding between anchors.

Acknowledgements

This work was funded by an equipment grant from Natural Sciences and Engineering Research Council of Canada (NSERC) and Smart Underground Mining and Integrated Technology program (SUMIT) funded by the Ontario Research Fund (ORF).

References

1 McKinnon SD. Triggering of seismicity remote from active mining excavations. *Rock Mech Rock Eng*. 2006;39(3):255–279.
2 Wang G, Kaiser PK, Vasak P. Modeling of mining-induced seismicity migration. In: *ROCKENG09: Proceedings of the 3rd CANUS Rock Mechanics Symposium*. Toronto; 2009: Paper 4002.
3 Kaiser P.K., Vasak P., Suorineni F.T., Thibodeau D. New dimensions in seismic data interpretation with 3-D virtual reality visualization for burst-prone mines. In: *Proceedings of the 6th International Symp. on Rockburst and Seismicity in Mines (RaSiM6)*. Perth: 2005: 33–45.
4 Trifu C-I, Urbancic TI. Fracture coalescence as a mechanism for earthquakes: observations based on mining induced microseismicity. *Tectonophysics*. 1996;261(1–3):193–207.
5 Cole C. Longitudinal Train DynamicsIwnicki S, ed. Handbook of Railway Vehicle Dynamics, Boca Raton, FL: CRC Press Taylor & Francis Group; 2006, pp.239–277.
6 Burridge R, Knopoff L. Model and theoretical seismicity. *Bull Seismol Soc Am*. 1967;57(3):341–371.
7 Thévenaz L, Facchini M, Fellay A, Nikles M, Robert P. Field tests of distributed temperature and strain measurement for smart structures. In: *Proceedings of the 4th Pacific Rim Conference on Lasers and Electro-Optics. Chiba*. Japan: IEEE; 2001: 490–491.
8 Inaudi D, Glišić B. Distributed fiber optic strain and temperature sensing for structural health monitoring. In: *IABMAS'06 Proceedings of the 3rd International'l Conference on Bridge Maintenance, Safety and Management*. Porto: CRC Press Taylor & Francis Group; 2006: 8.
9 Inaudi D, Glišić B. Integration of distributed strain and temperature sensors in composite coiled tubing. In: *Proc. SPIE 6167, Smart Structures and Materials 2006: Smart Sensor Monitoring Systems and Applications*. San Diego, CA: SPIE; 2006: 616717.
10 He J, Zhou Z, Jinping O. Optic fiber sensor-based smart bridge cable with functionality of self-sensing. *Mech Syst Signal Process*. 2012;35(1–2):84–94.
11 Glišić B, Chen J, Hubbell D. Streicker Bridge: A comparison between Bragg-grating long-gauge strain and temperature sensors and Brillouin scattering-based distributed strain and temperature sensors. In: *Proc. SPIE 7981, Sensors and Smart Structures Technologies for Civil, Mechanical, and Aerospace Systems*. San Diego, CA: SPIE; 2011: 79812C
12 Glišić B, Posenato D, Inaudi D. Integrity monitoring of old steel bridge using fiber optic distributed sensors based on Brillouin scattering. In: *Proc. SPIE 6531, Nondestructive Characterization for Composite Materials, Aerospace Engineering, Civil Infrastructure, and Homeland Security*. San Diego, CA: SPIE; 2007: 65310P
13 Murayama H, Kageyama K. Application of fiber-optic distributed sensors to health monitoring for full-scale composite structures. *J Intell Mater Syst Struct*. 2003;14(1):3–13.
14 Zhu P, Leng YB, Zhou Y, Jiang GL. Safety inspection strategy for earth embankment dams using fully distributed sensing. *Procedia Eng*. 2011;8:520–526.
15 Hoepffner R, Singer J, Thuro K, Aufleger M. Development of an integral system for dam and landslide monitoring based on distributed fibre optic technology. In: *Proceedings of the 15th Biennial Conference on Ensuring Reservoir Safety into the Future*. 2008: 12.
16 Iten M, Hauswirth D, Puzrin AM. Distributed fiber optic sensor development, testing and evaluation for geotechnical monitoring applications. In: *Proc. of SPIE Vol. 7982 Smart Sensor Phenomena, Technology, Networks, and Systems 2011*. San Diego, CA: SPIE; 2011: 798207.
17 Mohamad H, Bennett P, Soga K. et al. Monitoring Tunnel Deformation Induced by Close-Proximity Bored Tunneling Using Distributed Optical Fiber Strain Measurements. In: *Proceedings of the 7th FMGM 2007: Field Measurements in Geomechanics*. Boston, MA: American Society of Civil Engineers; 2007: 1–13.
18 Naruse H, Uehara H, Deguchi T. et al. Underground mine monitoring using distributed fiber optic strain sensing system. In: *Optical Fiber Sensors. OSA Technical Digest (CD)*. Cancun; 2006.
19 Moffat RA, Sotomayor J, Beltrán JF. Estimating tunnel wall displacements using a simple sensor based on a Brillouin optical time domain reflectometer apparatus. *Int J Rock Mech Min Sci*. 2015;75:233–243.
20 Moffat RA, Beltran JF, Herrera R. Applications of BOTDR fiber optics technology to the monitoring of underground structures. *Geomech Eng*. 2016;9(3):397–414.
21 Thévenaz L. Brillouin distributed time-domain sensing in optical fibers: state of the art and perspectives. *Front Optoelectron China*. 2010;3(1):13–21.
22 Thévenaz L, Nikles M, Fellay A, Facchini M, Robert P.A. Applications of distributed Brillouin fiber sensing. In: *Proceedings of the SPIE 3407, International Conference on Applied Optical Metrology*. Balatonfured, Hungary; 1998: 374–381.
23 Adachi JI, Detournay E. Plane strain propagation of a hydraulic fracture in a permeable rock. *Eng Fract Mech*. 2008;75(16):4666–4694.
24 Valley B, Madjdabadi B, Kaiser PK, Dusseault MB. Monitoring mining-induced rock mass deformation using distributed strain monitoring based on fiber optics. In: *European Rock Mechanics Symposium-EUROCK 2012*. Stockholm; 2012: 14.
25 Madjdabadi B, Valley B, Dusseault MB, Kaiser PK. Experimental evaluation of a distributed Brillouin sensing system for measuring extensional and shear deformation in rock. *Measurement*. 2016;77:54–66.
26 Minardo A, Bernini R, Amato L, Zeni L. Bridge Monitoring Using Brillouin Fiber-Optic Sensors. *IEEE Sens J*. 2012;12(1):145–150.
27 Hoepffner R. Distributed fiber optic strain sensing in hydraulic concrete and earth structures: measuring theory and field investigations on dams and landslides [Ph.D. Thesis], Munich: Technische Universität München; 2008.
28 Ansari BF, Libo Y. Mechanics of bond and interface shear transfer in optical. *J Eng Mech*. 1998;124(4):385–394.
29 Wan KT, Leung CKY, Olson NG. Investigation of the strain transfer for surface-attached optical fiber strain sensors. *Smart Mater Struct*. 2008;17(3):035037.
30 Dunnicliff J. Geotechnical instrumentation for monitoring field performance, New York: Wiley; 1993.
31 Mikkelsen P. Cement-bentonite grout backfill for borehole instruments. *Geotech Instrum News*. 2002;20(4):38–42.